EFFECTS OF GALAXY FORMATION ON THERMODYNAMICS OF THE INTRACLUSTER MEDIUM

DAISUKE NAGAI,[1] ANDREY V. KRAVTSOV,[2] AND ALEXEY VIKHLININ[3,4]

ABSTRACT

We present detailed comparisons of the intracluster medium (ICM) in cosmological Eulerian cluster simulations with deep *Chandra* observations of nearby relaxed clusters. To assess the impact of galaxy formation, we compare two sets of simulations, one performed in the nonradiative regime and another with radiative cooling and several physical processes critical to various aspects of galaxy formation: star formation, metal enrichment, and stellar feedback. We show that the observed ICM properties outside cluster cores are well reproduced in the simulations that include cooling and star formation, while the nonradiative simulations predict an overall shape of the ICM profiles inconsistent with observations. In particular, we find that the ICM entropy in our runs with cooling is enhanced to the observed levels at radii as large as half of the virial radius. We also find that outside cluster cores entropy scaling with the mean ICM temperature in both simulations and *Chandra* observations is consistent with being self-similar within current error bars. We find that the pressure profiles of simulated clusters are also close to self-similar and exhibit little cluster-to-cluster scatter. We provide analytic fitting formulae for the pressure profiles of the simulated and observed clusters. The X-ray observable mass relations for our simulated sample agree with the *Chandra* measurements to $\approx 10\%$–20% in normalization. We show that this systematic difference could be caused by the subsonic gas motions, unaccounted for in X-ray hydrostatic mass estimates. The much improved agreement of simulations and observations in the ICM profiles and scaling relations is encouraging, and the existence of tight relations of X-ray observables, such as Y_X, and total cluster mass and the simple redshift evolution of these relations hold promise for the use of clusters as cosmological probes. However, the disagreement between the predicted and observed fractions of cluster baryons in stars remains a major puzzle.

Subject headings: cosmology: theory — galaxies: clusters: general — methods: numerical

Online material: color figures

1. INTRODUCTION

Clusters of galaxies are fascinating astrophysical objects and laboratories for studying galaxy formation and structure formation in general. At the same time, clusters can provide cosmological constraints that are complementary to those obtained with other methods such as temperature anisotropies of the cosmic microwave background, Type Ia supernovae, and weak lensing (e.g., Voit 2005; Tozzi 2006; Borgani 2006; Albrecht et al. 2006). Cosmological applications of clusters include cluster counts and their evolution with redshift (e.g., Henry & Arnaud 1991; Markevitch 1998; Ikebe et al. 2002; Vikhlinin et al. 2003), spatial distribution (e.g., Miller et al. 2002), and the angular diameter distance measurements (Allen et al. 2004; LaRoque et al. 2006). Detailed observations of merging clusters provide unique insights into the physics of the intracluster plasma (e.g., Vikhlinin et al. 2001a, 2001b; Markevitch et al. 2003) and provide key evidence for the existence and properties of dark matter (Markevitch et al. 2004; Clowe et al. 2006).

All cosmological applications of clusters, at least to a certain degree, rely on solid understanding of the physics of their formation. Given that clusters are nonlinear collapsed systems, numerical cosmological simulations are the method of choice for their theoretical studies. Modern cosmological codes using *N*-body and numerical hydrodynamics techniques can accurately follow dynamics of dark matter and gaseous baryonic components in their full complexity during the hierarchical buildup of structures. Yet more realistic modeling of clusters requires inclusion of additional baryonic processes. For example, to model formation of cluster galaxies, we need, at the very least, to correctly treat energy dissipation due to radiative losses by baryons and conversion of gas into stars. In addition, any feedback in the form of energy injection and metal enrichment from supernova winds (e.g., Metzler & Evrard 1994; Valdarnini 2003) and active galactic nuclei (Brüggen et al. 2005; Sijacki & Springel 2006; Cattaneo & Teyssier 2007), and injection of nonthermal cosmic rays at large-scale shocks accompanying cluster formation (Pfrommer et al. 2007) can alter the thermodynamics of the intracluster gas.

Although our understanding of details and relative importance of these processes is currently sketchy, the simulations with specific assumptions about them are highly predictive, which should make models falsifiable. In particular, by comparing observed cluster properties with the results of simulations that include various physical processes described above we can learn a great deal about these processes and their role in cluster formation.

Over the last two decades, such comparisons were used extensively to put constraints on the deviations of ICM thermodynamics from the simple self-similar behavior, described originally by Kaiser (1986, 1991). The first studies of the observed correlation of cluster X-ray luminosity, L_X, and spectral temperature, T_X, unambiguously showed that its slope is steeper than the slope predicted by the self-similar model (e.g., Edge & Stewart 1991; Henry & Arnaud 1991; White et al. 1997; Markevitch 1998; Allen & Fabian 1998; Arnaud & Evrard 1999). In addition, the slope of the L_X-T_X relation steepens for the lowest mass clusters (e.g.,

[1] Theoretical Astrophysics, California Institute of Technology, Mail Code 130-33, Pasadena, CA 91125; daisuke@caltech.edu.
[2] Department of Astronomy and Astrophysics, Kavli Institute for Cosmological Physics, Enrico Fermi Institute, 5640 South Ellis Avenue, University of Chicago, Chicago, IL 60637.
[3] Harvard-Smithsonian Center for Astrophysics, 60 Garden Street, Cambridge, MA 02138.
[4] Space Research Institute, 84/32 Profsojuznaya Street, GSP-7, Moscow 117997, Russia.

Helsdon & Ponman 2000; Finoguenov et al. 2002, 2007). Deviations from self-similarity were shown to be the strongest in the cores of clusters (e.g., Markevitch 1998; De Grandi & Molendi 2002; Vikhlinin et al. 2006) and were widely interpreted as evidence for preheating of the intracluster gas by energy from supernovae and AGN feedback (e.g., David et al. 1991; Kaiser 1991; Evrard & Henry 1991; White 1991; Wu et al. 2000; Bialek et al. 2001; Borgani et al. 2001, 2002; Nath & Roychowdhury 2002).

Alternative explanation was proposed by Bryan (2000), who argued that cooling and condensation of the gas accompanying formation of cluster galaxies can reduce the ICM gas density and increase its temperature and entropy to the observed levels (see also Voit & Bryan 2001; Voit et al. 2002). This explanation was borne out by cosmological simulations (Pearce et al. 2000; Muanwong et al. 2001; Valdarnini 2002; Davé et al. 2002; Kay et al. 2004, 2007). However, the amount of gas that condenses out of the hot ICM in cosmological simulations due to cooling (e.g., Suginohara & Ostriker 1998; Lewis et al. 2000; Pearce et al. 2000; Davé et al. 2002; Ettori et al. 2004) appears to be a factor of 2–3 too large compared to the observed stellar mass in clusters (Lin et al. 2003; Gonzalez et al. 2007). Thus, the X-ray measurements appear to be consistent with a large fraction of cooling gas, while the optical estimates of stellar mass indicate that this fraction is small.

Modern X-ray observations with *Chandra* and *XMM-Newton* allow us to study the ICM properties with unprecedented detail and accuracy. Their superb spatial resolution and sensitivity enable resolved, accurate X-ray brightness and temperature maps over a large fraction of the cluster virial radii. The X-ray measurements also enable accurate mass modeling of relaxed clusters with the assumption of hydrostatic equilibrium of the ICM in the cluster potential. These observations can therefore be used for detailed comparisons of both global cluster properties and their profiles with simulation results, which provide more stringent tests for the models of the ICM thermodynamics. In particular, such comparisons can shed some light on the apparently contradictory lines of evidence as to the efficiency of cooling in clusters described above.

To this end, in the present study we focus on the effects of radiative cooling and star formation on the observable properties of clusters and compare results of simulations in both nonradiative and radiative regimes with the current X-ray data. Namely, we use two sets of simulations started from the same initial conditions. Both sets treat collisionless dynamics of dark matter and hydrodynamics of diffuse gas with high resolution using the adaptive mesh refinement technique. In the baseline set of cluster simulations, the gas is modeled in nonradiative regime and thus does not reach high densities and is not allowed to form stars. The second set of simulations includes several processes accompanying galaxy formation: gas cooling, star formation, metal enrichment, and thermal feedback due to the supernovae. Comparison of the simulated profiles in these two sets of simulations to those of observed clusters allows us to gauge the role of galaxy formation in shaping properties of the ICM. As we show in § 4, the simulations that include galaxy formation processes provide a considerably better match to the observed ICM profiles outside cluster cores compared to the nonradiative simulations.

The paper is organized as follows. In § 2 we describe cosmological cluster simulations. The methods used to analyze the simulations and the brief description of observations used in our comparisons are given in §§ 2 and 3, respectively. We present results of comparison of the ICM density, temperature, entropy, and pressure profiles in § 4, and integrated quantities such as spectral X-ray gas temperature, gas mass, and pressure, in simulations

and observations in § 5. We discuss our results and conclusions in § 6.

2. COSMOLOGICAL CLUSTER SIMULATIONS

In this study, we analyze high-resolution cosmological simulations of 16 cluster-sized systems in the flat ΛCDM model: $\Omega_m = 1 - \Omega_\Lambda = 0.3$, $\Omega_b = 0.04286$, $h = 0.7$, and $\sigma_8 = 0.9$, where the Hubble constant is defined as $100\ h$ km s^{-1} Mpc^{-1}, and an σ_8 is the power spectrum normalization on an $8\ h^{-1}$ Mpc scale. The simulations were done with the Adaptive Refinement Tree (ART) N-body+gas dynamics code (Kravtsov 1999, 2002), an Eulerian code that uses adaptive refinement in space and time, and (nonadaptive) refinement in mass (Klypin et al. 2001) to reach the high dynamic range required to resolve cores of halos formed in self-consistent cosmological simulations. The same set of cluster simulations was used in our related recent studies (Kravtsov et al. 2006; Nagai et al. 2007), where additional details can be found. We provide a description of the simulation details here for completeness.

The N-body+gas dynamics cluster simulations used in this analysis follow collisionless dynamics of dark matter and stars, gas dynamics, and several physical processes critical to various aspects of galaxy formation: star formation, metal enrichment and thermal feedback due to Type II and Type Ia supernovae, self-consistent advection of metals, metallicity-dependent radiative cooling, and UV heating due to cosmological ionizing background (Haardt & Madau 1996). The cooling and heating rates take into account Compton heating and cooling of plasma, UV heating, and atomic and molecular cooling, and are tabulated for the temperature range $10^2 < T < 10^9$ K and a grid of metallicities and UV intensities using the Cloudy code (ver. 96b4; Ferland et al. 1998). The Cloudy cooling and heating rates take into account metallicity of the gas, which is calculated self-consistently in the simulation, so that the local cooling rates depend on the local metallicity of the gas. Star formation in these simulations was done using the observationally motivated recipe (e.g., Kennicutt 1998): $\dot{\rho}_* = \rho_g^{1.5}/t_*$, with $t_* = 4 \times 10^9$ yr. Stars are allowed to form in regions with temperature $T < 2 \times 10^4$ K and gas density $n > 0.1$ cm^{-3}.[5] The code also accounts for the stellar feedback on the surrounding gas, including injection of energy and heavy elements (metals) via stellar winds, supernovae, and secular mass loss. The details of star formation prescription and feedback are discussed in Kravtsov et al. (2005). Some potentially relevant physical processes, such as AGN bubbles, physical viscosity, magnetic field, and cosmic rays, are not included.

The adaptive mesh refinement technique is used to achieve high spatial resolution in order to follow the galaxy formation and evolution self-consistently in these simulations. The peak spatial resolution is ≈ 7 and $5\ h^{-1}$ kpc, and the dark matter particle mass in the region around the cluster was 9.1×10^8 and $2.7 \times 10^8\ h^{-1}\ M_\odot$ for CL 101–107 and CL 3–24, respectively. To test the effects of galaxy formation, we also repeated each cluster simulation with only the standard gas dynamics for the baryonic component, without radiative cooling or star formation. We will use labels "nonradiative" and "cooling+SF" (CSF) to refer to these two sets of runs, respectively.

In this work, we also use mock *Chandra* X-ray images and spectra of the simulated clusters to derive total mass, gas mass, and

---

[5] We have compared runs where star formation was allowed to proceed in regions different from our fiducial runs. We considered thresholds for star formation of $n = 10, 1, 0.1$, and 0.01 cm^{-3}. We find that thresholds affect the properties of the ICM at small radii, $r/r_{\rm vir} < 0.1$, but differences are negligible at the radii we consider in this study.

TABLE 1
Simulated Cluster Sample of the CSF Run at $z = 0$

Name	r_{500} (h^{-1} Mpc)	M_{500}^{gas} (h^{-1} 10^{13} $M_\odot$)	M_{500}^{tot} (h^{-1} 10^{13} $M_\odot$)	T_{mg}^{SIM} (keV)[a]	T_X (keV)[b]			Relaxed/Unrelaxed[c]
					x	y	z	
CL 101	1.160	8.17	90.81	7.44	8.72	8.67	8.86	000
CL 102	0.978	4.82	54.47	5.63	5.63	5.83	5.86	000
CL 103	0.994	4.92	57.71	4.84	4.73	4.93	4.62	000
CL 104	0.976	5.15	53.88	6.61	7.69	7.73	7.73	111
CL 105	0.943	4.71	48.59	5.67	6.21	6.21	6.17	001
CL 106	0.842	3.17	34.65	4.54	4.34	4.35	4.30	000
CL 107	0.762	2.17	25.66	3.61	3.97	3.71	3.94	100
CL 3	0.711	1.91	20.90	3.37	3.65	3.60	3.61	111
CL 5	0.609	1.06	13.11	2.22	2.40	2.39	2.39	111
CL 6	0.661	1.38	16.82	2.88	3.38	3.38	3.57	000
CL 7	0.624	1.21	14.13	2.54	2.96	2.88	2.90	111
CL 9	0.522	0.73	8.23	1.58	1.53	1.60	1.57	000
CL 10	0.487	0.43	6.72	1.58	1.93	1.90	1.91	111
CL 11	0.537	0.78	8.99	1.75	2.00	2.02	1.98	000
CL 14	0.509	0.62	7.69	1.64	1.85	1.84	1.83	111
CL 24	0.391	0.26	3.47	0.97	1.06	1.04	1.07	010

[a] T_{mg}^{SIM} is the average temperature measured directly from the 3D ICM distribution in the simulations.
[b] Average temperatures measured in the shell of $[0.15, 1]r_{500}$ from the mock *Chandra* analysis of simulated clusters viewed along three orthogonal projection axes (x, y, and z, from left to right). Note that the values of T_X quoted here are different from those in Table 1 of Nagai et al. (2007) where erroneous values were presented.
[c] Classification of relaxed and unrelaxed clusters are indicated with 0 and 1, respectively, for the three projections.

temperature profiles, as well as integrated cluster properties using the analysis procedures essentially identical to those used to analyze real *Chandra* observations, as described in Nagai et al. (2007). The average X-ray spectral temperature, T_X, is obtained from a single-temperature fit to the spectrum integrated within r_{500}, excluding the central region, $r < 0.15r_{500}$. For each cluster, the mock data is created for three orthogonal projections along the x, y, and z coordinate axes. In § 5.3 we use quantities derived from the mock observations to compare scaling relations exhibited by simulated clusters to observations.

Our simulated sample includes 16 clusters at $z = 0$ and their most massive progenitors at $z = 0.6$. The properties of simulated clusters at $z = 0$ are given in Table 1. The masses are reported at the radius r_{500} enclosing overdensities with respect to the critical density at the redshift of the output. This choice of the outer radius is mainly motivated by the fact that clusters are more relaxed within r_{500} compared to the outer regions (Evrard et al. 1996). We also use r_{200}, r_{1000}, and r_{2500}, which are approximately 1.52, 0.71, and 0.44 times r_{500}, respectively. Mean spectral temperatures are presented separately for the three orthogonal projections to show the variation due to projection effects, substructure, etc. Note that the values of T_X quoted here are different from those in Table 1 of Nagai et al. (2007), where erroneous values were presented by mistake. In our analysis below we distinguish unrelaxed and relaxed clusters for a more consistent comparison with the observations. The classification is based on the overall morphology of the mock X-ray images, as discussed in Nagai et al. (2007). In Table 1 relaxed and unrelaxed clusters are indicated with 0 and 1 for the three orthogonal projections (x, y, z, from left to right).

3. OBSERVATIONAL CLUSTER SAMPLE

To test our simulation results against observations we use a set of accurate measurements of gas density, temperature, and total mass profiles for a subsample of 13 relaxed clusters at $z \sim 0$ that was presented in Vikhlinin et al. (2005, 2006). The clusters are selected on the basis of regular and relaxed morphology of their X-ray surface brightness images, although some of the systems show signs of AGN activity in their cores. Three of the low-T_X

clusters, including USGC S152 ($T_X = 0.69$ keV), A262 ($T_X = 1.89$ keV), and RX J1159+5531 ($T_X = 1.80$ keV), are excluded from the comparisons that involve measurements of M_{500} or normalization with r_{500}, because their values are very uncertain due to insufficient spatial coverage. In § 5.2, we include USGC S152 and RX J1159+5531 for comparisons of the entropy scaling relations at $0.1r_{200}$, r_{2500}, and r_{1000}, and A262 at the first two radii, but not at r_{1000}. Since none of the measurements extends out to r_{200}, we estimate r_{200} using $r_{200} = 1.52r_{500}$, which provides a robust and accurate estimate of r_{200} for our CSF and nonradiative simulations, as well as the *XMM-Newton* mass measurements (Pointecouteau et al. 2005). The observations and analysis procedure used to extract ICM properties and profiles from the *Chandra* data are described in detail in Vikhlinin et al. (2005, 2006).

In our previous study (Nagai et al. 2007), we used the mock *Chandra* images and spectra of the simulated clusters to assess the accuracy of the X-ray measurements of galaxy cluster properties. Our results show that the X-ray analysis of Vikhlinin et al. (2006) provides a very accurate reconstruction of the 3D gas density and temperature profiles for relaxed clusters. Therefore, we directly compare the profiles derived from *Chandra* analysis to the 3D profiles of simulated clusters. Note that masses and overdensity radii of the clusters in the *Chandra* sample were derived from the X-ray hydrostatic analysis. A bias in the estimated cluster mass may results in a slight underestimate of the estimated cluster virial radius r_{500}^{est} by about a few percent for relaxed clusters (see also Nagai et al. 2007, for more details and discussions). We will show such a comparison in § 4.

At the same time, our tests show that X-ray analysis can result in a $\approx 15\%$ underestimate in the hydrostatic estimates of total cluster mass. The bias is due to the nonthermal pressure support from the subsonic turbulent motions of the ICM gas, ubiquitous in cluster simulations (Evrard 1990; Norman & Bryan 1999; Nagai et al. 2003, 2007; Rasia et al. 2004, 2006; Kay et al. 2004; Faltenbacher et al. 2005; Dolag et al. 2005), but not included in observational hydrostatic mass estimates. In § 5.3, we present the comparisons of the X-ray observable mass relations of our simulated clusters to deep *Chandra* X-ray observations of nearby, relaxed clusters

using both the true masses of clusters measured in simulations and the masses estimated from hydrostatic equilibrium analysis. We also correct for the differences in the assumed cosmological parameters in simulations ($f_b \equiv \Omega_B/\Omega_M = 0.1429$ and $h = 0.7$) to those assumed in the observational analyses ($f_b = 0.175$ and $h = 0.72$). We adopt $f_b = 0.175$ and $h = 0.7$ throughout this work. Note that $\Omega_M = 0.3$ and $\Omega_\Lambda = 0.7$ are assumed in both analyses.

In addition, we compare in § 5.2 the *Chandra* ICM entropy measurements with those based on the *XMM-Newton* observations of 10 clusters (Pratt et al. 2006) and the *ROSAT+ASCA* data for 64 clusters (Ponman et al. 2003). In these comparisons, we do not use measurements that involve extrapolation, so that we minimize biases arising from such procedure.

4. EFFECTS OF GALAXY FORMATION ON THE ICM PROFILES

In this section we investigate the effects of galaxy formation on the ICM properties by comparing simulations performed with and without the processes associated with the galaxy formation: gas cooling, star formation, stellar feedback, and metal enrichment. Similar comparisons have been done for a subset of 11 clusters in Kravtsov et al. (2005) and Nagai (2006). Here, we use the extended sample of 16 clusters and analyze the subsample of six relaxed clusters that are identified as "relaxed" in all three orthogonal projections, indicated as 111 in the last column of the Table 1. In § 5, we compare the results of simulations to the *Chandra* X-ray observations of nearby relaxed clusters.

Figure 1 shows the average radial profiles of the ICM in relaxed clusters at $z = 0$ in the CSF and nonradiative runs. Clockwise from the top left panel, we show the gas density, temperature, pressure, and entropy profiles. The mean profiles are obtained by first normalizing the ICM profiles of each cluster at r_{500} and then averaging over a sample of relaxed clusters. The shaded bands show 1 σ rms scatter around the mean profile of the CSF runs, and the mean and scatter of the profiles are computed for a logarithm of each thermodynamic quantity. We also examine systems with $T_X > 2.5$ keV and <2.5 keV separately to study the mass dependence of the effects (and also the effects of cooling in the bremsstrahlung- and line emission–dominated regimes). In the bottom panel of each figure, we also show the fractional change of the ICM profiles in the CSF runs relative to the nonradiative runs.

The temperature, entropy (defined as $K \equiv k_B T/n_e^{2/3}$), and pressure profiles are normalized to the values computed for the given cluster mass using a simple self-similar model (Kaiser 1986; Voit 2005):

$$T_{500} = 11.05 \text{ keV} \left(\frac{M_{500}}{10^{15}\ h^{-1}\ M_\odot}\right)^{2/3} E(z)^{2/3}, \quad (1)$$

$$K_{500} = 1963 \text{ keV cm}^{-2} \left(\frac{M_{500}}{10^{15}\ h^{-1}\ M_\odot}\right)^{2/3} E(z)^{-2/3}, \quad (2)$$

$$P_{500} = 1.45 \times 10^{-11} \text{ erg cm}^{-3}$$
$$\times \left(\frac{M_{500}}{10^{15}\ h^{-1}\ M_\odot}\right)^{2/3} E(z)^{8/3}, \quad (3)$$

where M_{500} is a total cluster mass enclosed within r_{500} and $E^2(z) = \Omega_M(1+z)^3 + \Omega_\Lambda$ for a flat universe with a cosmological constant assumed in our simulations. Numerical coefficients in equations (2) and (3) follow from the definitions $K_{500} \equiv k_B T_{500}/n_{e,500}^{2/3}$ and $P_{500} \equiv n_{g,500} k_B T_{500}$, where $n_{e,500} =$

$(\mu/\mu_e)n_{g,500} = 500 f_b \rho_{\rm crit}/(\mu_e m_p)$, $\rho_{\rm crit}$ is the critical density of the universe, $f_b \equiv \Omega_M/\Omega_b$ is the mean baryon fraction in the universe, μ is the mean molecular weight, and μ_e is the mean molecular weight per free electrons. Note that we use $\mu = 0.59$ and $\mu_e = 1.14$ throughout this work.

Figure 1 shows that including the gas cooling and star formation significantly modifies the ICM profiles throughout the cluster volume. The effect is larger in the inner region and for the systems with lower T_X (or the cluster mass). Compared to the nonradiative runs, the gas density in the CSF runs is reduced by $\approx 50\%$ and 25% at 0.3 and 1.0 r_{500}, because a fraction of gas is converted into stars. At small radii, we observe a trend with cluster mass; for example, the suppression of the gas density in the CSF runs at $r = 0.1 r_{500}$ is $\sim 50\%$ and 30% for systems with $T_X < 2.5$ keV and >2.5 keV, respectively. However, at $r > 0.3 r_{500}$ (or $r > 0.15 r_{\rm vir}$), our simulations show very little systematic trend with T_X, indicating that the clusters become self-similar in the outskirts even when the cooling and star formation are turned on.

The ICM temperature profiles decline monotonically from $0.05 r_{500}$ outwards. The shape of the temperature profiles are similar between the nonradiative and CSF runs, but there is a clear offset in their normalization. The temperature in the CSF runs is systematically higher by 10%–20% outside the core, indicating that the net effect of gas cooling and star formation is to increase the ICM temperature. The effects of gas cooling and star formation on the ICM temperature show a stronger dependence on cluster mass than gas density.

The ICM entropy provides one of the most fundamental insights into physical processes determining the thermodynamics of the ICM, because it is expected to a be a conserved quantity, modified only by shock waves and "nonadiabatic" processes we are interested in (e.g., see Voit et al. 2002, 2005, and references therein). Figure 1 shows that the entropy profiles in our nonradiative simulations scale self-similarly and are well described by a power law $K \propto r^{1.2}$, at $r > 0.3 r_{500}$, in agreement with previous studies (Voit et al. 2005). Note, however, that there is a systematic discrepancy between the predictions of the Eulerian and SPH codes at small radii (Frenk et al. 1999; Ascasibar et al. 2003). However, since the primary focus of this paper is on the ICM properties outside the cluster core, we leave a detailed analysis of this entropy discrepancy for future work.

Using the average $K(r)$ profile from the nonradiative simulations as a baseline, we study the effects of gas cooling and star formation on the ICM entropy. Compared to the nonradiative runs, the ICM entropy in the CSF runs is enhanced in the entire radial range of interest, even at the virial radius $r_{\rm vir} \simeq 2 r_{500}$. This is because cooling leads to the condensation of the lowest entropy gas, which is replaced by the gas of higher entropy (Bryan 2000; Voit & Bryan 2001). The effect strongly depends on radius and is most pronounced in the inner regions with the largest effect of $\sim 100\%$ near $r = 0.3 r_{500}$. However, the entropy is enhanced by $\sim 40\%$ even at $r = r_{500}$. The figure also shows that the magnitude of the effect in the inner regions depends on cluster mass, but is approximately the same for all masses at $r \gtrsim 0.5 r_{500}$, indicating that cooling preserved self-similarity of the cluster outskirts.

Finally, pressure profiles exhibit the most remarkable degree of self-similarity and low level of cluster-to-cluster scatter. Notice that the average pressure profiles of low- and high-T_X systems are nearly identical. This indicates that the self-similarity is best preserved for the quantities directly proportional to the ICM pressure or thermal energy, such as the integrated pressure $Y_{\rm SZ} \propto M_g T_{\rm mg}$ (Nagai 2006) and $Y_X \equiv M_g T_X$ (Kravtsov et al. 2006). Note, however, that inclusion of gas cooling and star formation modifies the overall shape and normalization of the pressure
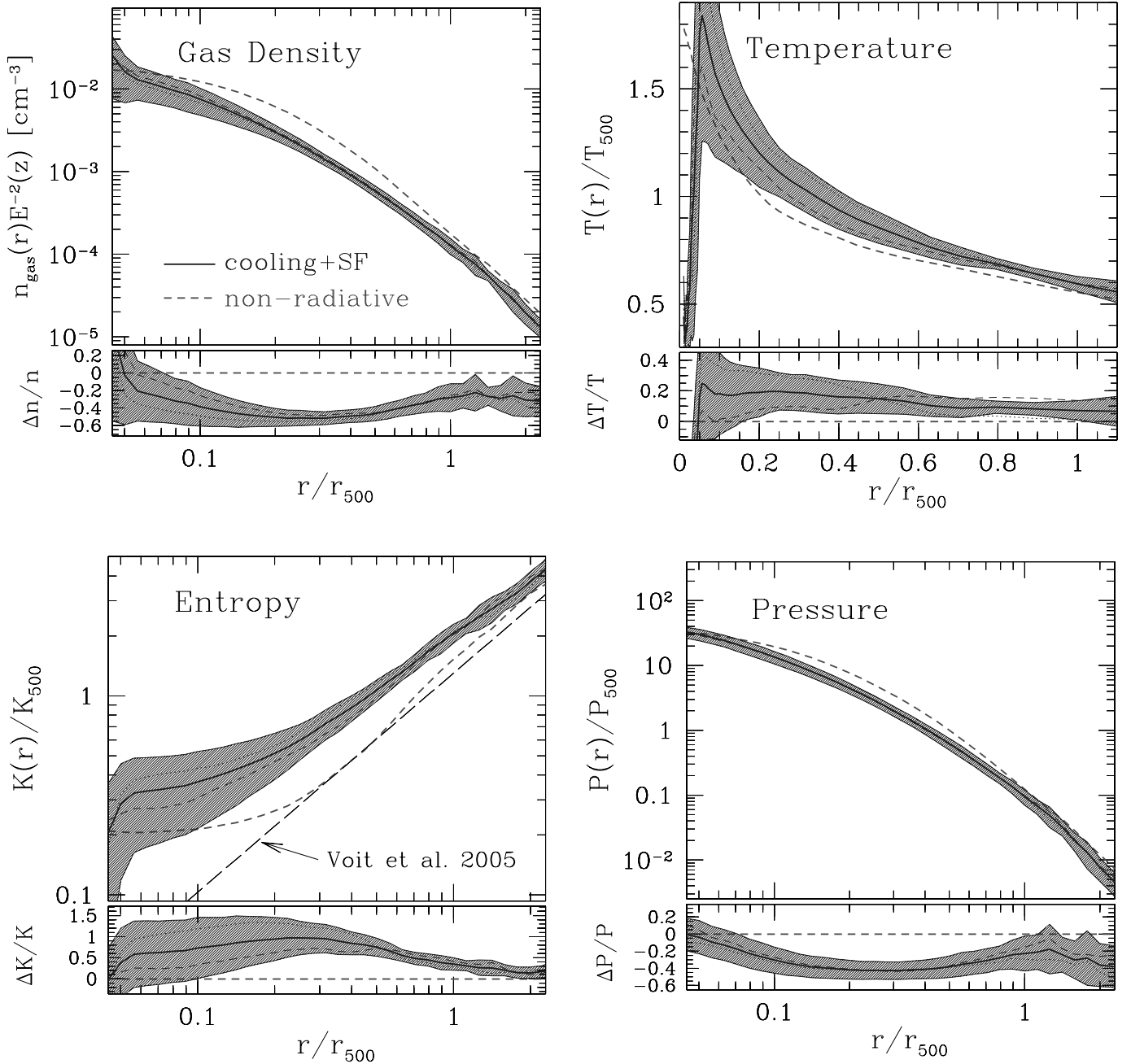
Fig. 1.—Radial profiles of the ICM in *relaxed* simulated clusters at $z = 0$. For each of the physical profiles the upper panels show the profiles, while the bottom panels show the corresponding fractional deviations of the profiles in the CSF simulation from the corresponding profiles in the nonradiative runs. The figure shows gas density (*top left*), temperature (*top right*), entropy (*bottom left*), and pressure (*bottom right*) profiles. Thick solid and dashed lines show the average profiles of the relaxed clusters in the CSF and nonradiative runs, respectively. The shaded band indicates the rms scatter around the mean profile for the CSF run. In addition, the dashed and dotted lines indicate the average profiles of systems with $T_X > 2.5$ and <2.5 keV, respectively, in the CSF simulations. Note that the entropy profiles of the nonradiative runs outside $0.3r_{500}$ are well described by a power-law radial profile $K \propto r^{1.2}$, indicated by the dashed line in the bottom left panel. [*See the electronic edition of the Journal for a color version of this figure.*]

profiles and hence the Y_{SZ} and Y_X parameters for the clusters of a fixed mass. In our simulations, the ICM pressure is suppressed by about 25% and 40% at r_{500} and r_{2500}, respectively.

5. COMPARISONS WITH OBSERVATIONS

In this section we present detailed comparisons of gas density, temperature, entropy, and pressure profiles in the simulated clusters and the *Chandra* observations of low-z relaxed clusters (Vikhlinin et al. 2006). We also compare the scaling relations between T_X, M_g, the X-ray "pressure" ($Y_X \equiv M_g T_X$), and cluster total mass.

5.1. *Profile Comparison*

Figure 2 compares the ICM profiles in simulations with those observed. For the simulated clusters, we plot the mean ICM profiles averaged over the samples of relaxed clusters in both non-radiative and CSF runs. They are compared to the *Chandra* X-ray measurements of 11 nearby relaxed clusters. The observed clusters with $T_X > 5$ keV, 2.5 keV $< T_X < 5$ keV, and $T_X > 5$ keV are indicated with thin dotted, long-dashed, and short-dashed lines.

The comparisons show that the ICM profiles in the CSF simulations agree quite well with observations outside the cores of
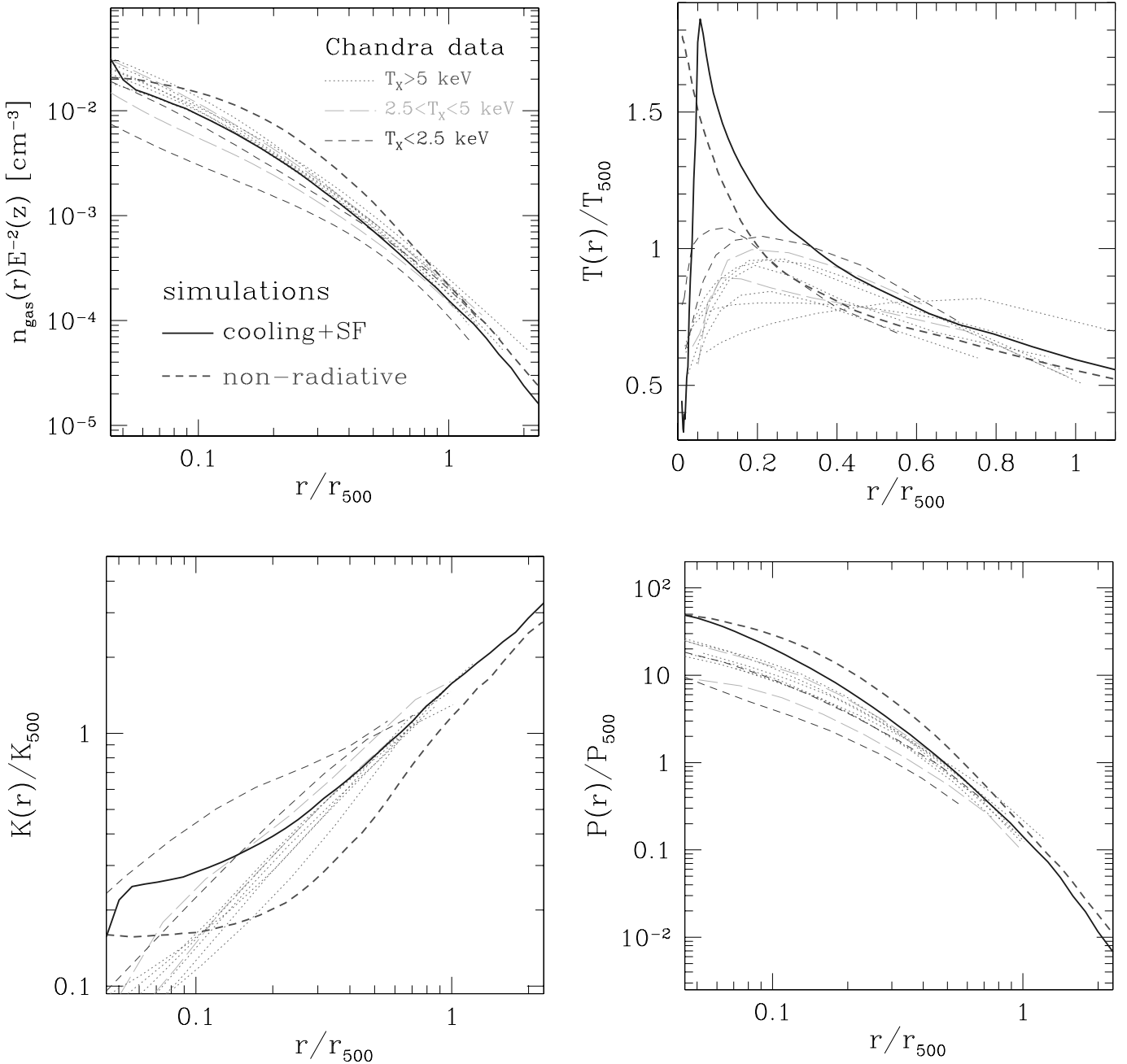
FIG. 2.—Comparison of the ICM profiles in relaxed clusters at the present day ($z \approx 0$) in cosmological cluster simulations and the *Chandra* sample of Vikhlinin et al. (2006). The panels show the gas density (*top left*), temperature (*top right*), entropy (*bottom left*), and pressure (*bottom right*). Thick solid and dashed lines show the mean profiles in the CSF and nonradiative simulations, respectively, while the observed profiles are shown by the thin dotted, long-dashed, and short-dashed lines for the systems with $T_X > 5$ keV, 2.5 keV $< T_X < 5$ keV, and $T_X < 2.5$ keV, respectively. Note that at $r \gtrsim 0.1 r_{500}$, the profiles of the CSF simulations provide a better match to the observed profiles than the profiles in the nonradiative runs. [*See the electronic edition of the Journal for a color version of this figure.*]

clusters ($r \gtrsim r_{2500}$), while the nonradiative simulations predict overall shape and normalization of the ICM profiles inconsistent with observations at all radii. The observations indicate then that a significant amount of cooling and condensation of gas out of hot ICM phase has occurred in real clusters.

The ICM profiles in the inner regions, on the other hand, are not reproduced well in any of our simulations. The only exception is the $n_g(r)$ profiles for $T_X > 5$ keV clusters, where the CSF runs produce results consistent with observation down to $r \simeq 0.06 r_{500}$. However, even for these clusters, the discrepancies between simulations and observations are evident in the $T(r)$ and $P(r)$ profiles at $r < 0.3 r_{500}$. The shape of the entropy profiles is

different in the inner region of the simulated and observed clusters. For example, the entropy profiles of the observed clusters monotonically decrease with decreasing radius, while simulated entropy profiles flatten substantially at $r \lesssim 0.2 r_{500}$.

Note that the ICM profiles of the $T_X < 2.5$ keV *Chandra* clusters are systematically offset from the high-T_X clusters in the inner regions and exhibit more pronounced cluster-to-cluster variations. The lowest T_X system, MKW4 ($T_X = 1.64$ keV), shows the most striking deviations from self-similarity. Our simulated clusters show similar trends, but the sample is too small to quantify the trends with T_X and the scatter. Note also that if we use the estimated r_{500} of simulated clusters to compare with data, the simulation
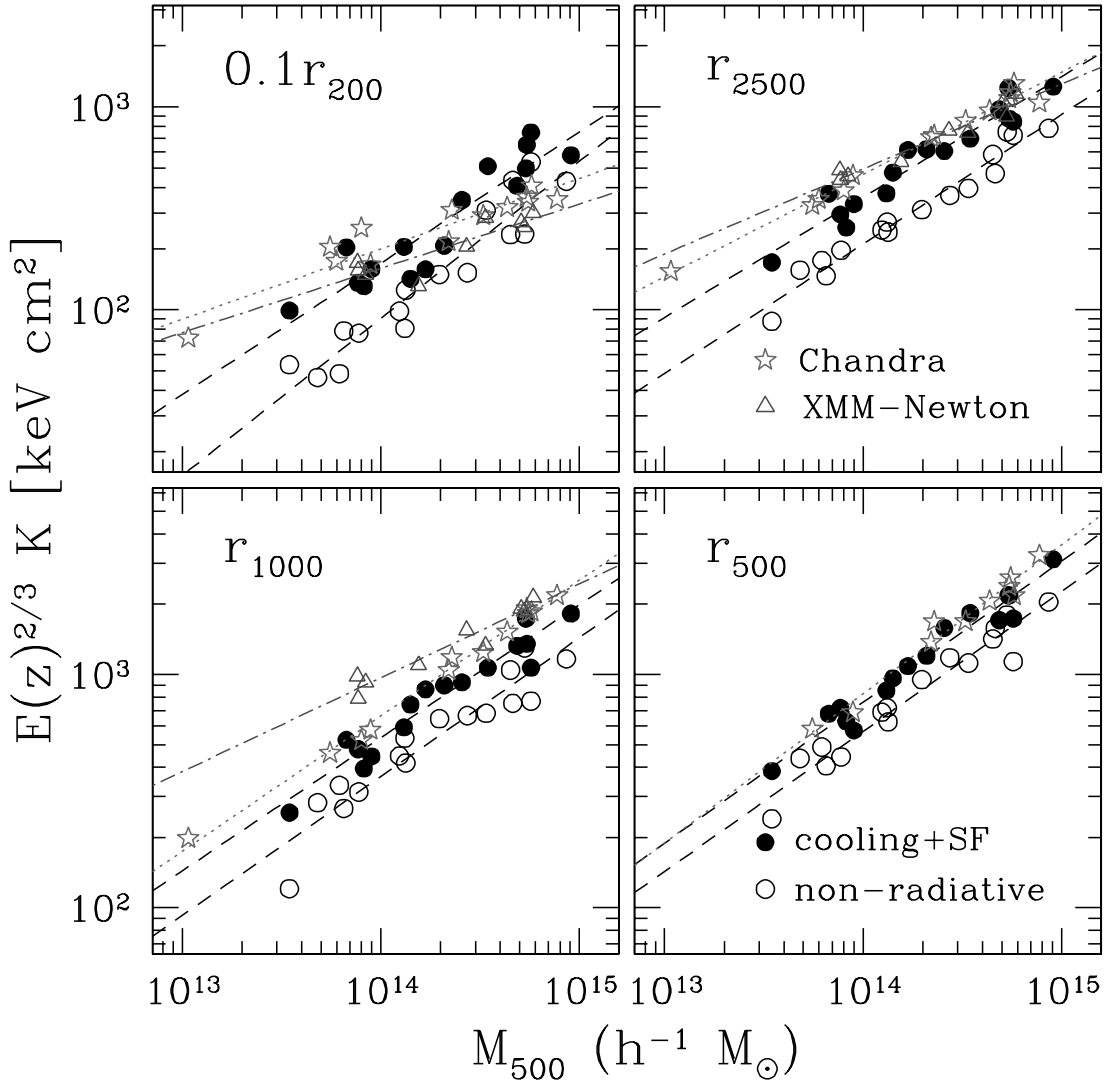
Fig. 3.—Correlation between the entropy $K \equiv k_B T / n_e^{2/3}$ as a function of M_{500}. The entropy scaling relations are measured at $0.1r_{200}$, r_{2500}, r_{1000}, and r_{500}. We compare the relations in the CSF and nonradiative simulations, indicated with filled and open circles , and the dashed and dotted lines indicate the best-fit power-law relations to these sets of simulations, respectively. Stars and triangles are observations by *Chandra* (Vikhlinin et al. 2006) and *XMM-Newton* (Pratt et al. 2006). The dashed lines indicate the best-fit power-law relations to the CSF (*upper line*) and nonradiative (*lower line*) simulations, while the dotted and dot-dashed lines indicate the fits to the *Chandra* and *XMM-Newton* measurements, respectively. [*See the electronic edition of the Journal for a color version of this figure.*]

curves in Figure 2 could slide to the left, bringing the characteristic values plotted in Figures 3 and 4 down slightly ($\lesssim 8\%$; see § 5.3 for more discussions).

5.2. *Entropy Scaling Relations*

The scaling of the entropy with mass or T_X of clusters provides one of the most powerful diagnostics of the effects of galaxy formation on the ICM and deviations from self-similarity (Evrard & Henry 1991; Ponman et al. 1999; Voit & Bryan 2001; Pratt et al. 2006). For the self-similar cluster model, the entropy at a fixed overdensity radius is expected to scale linearly with T_X and with mass as $\propto M^{2/3}$ (cf. eq. [1]). In the discussion above we showed that entropy profiles of both observed and simulated clusters become approximately self-similar outside the cluster cores. In this section we explicitly consider the scaling of entropy with cluster mass and temperature at four different radii and compare the results of numerical simulations with X-ray measurements obtained using *Chandra* (Vikhlinin et al. 2006). We also compare the *Chandra* measurements with the *XMM-Newton* (Pratt et al. 2006) and *ROSAT+ASCA* (Ponman et al. 2003) results.

The entropy levels measured in the simulated clusters at $0.1r_{200}$, r_{2500}, r_{1000}, and r_{500} are shown as a function of M_{500} in Figure 3 (such a relation was first studied observationally by Pratt et al. 2006). The best-fit power-law approximations of these data, $E(z)^{2/3} K = C(M_{500}/2 \times 10^{14}~h^{-1}~M_\odot)^\alpha$, are given in Table 2 [the $E(z)$ term corrects for evolution in the self-similar model, which needs to be applied to clusters observed at $z \neq 0$]. Clearly, in the simulated clusters, inclusion of gas cooling and star formation increases the entropy level, and the magnitude of the effect is larger in the inner region. The changes in the normalization for $M = 2 \times 10^{14}~h^{-1}~M_\odot$ clusters is a factor of 1.71, 1.65, 1.41, and 1.34 at $r = 0.1r_{200}$, r_{2500}, r_{1000}, and r_{500}, respectively. The effects of cooling and star formation on the ICM entropy are thus stronger at small radii. The slopes are consistent with the prediction of the self-similar model ($\alpha = 2/3$) within 1 σ at all radii, in both CSF and nonradiative simulations. However, there are indications that the slopes are slightly shallower than the self-similar value, and the slope in the nonradiative run is somewhat steeper than that in the CSF at $r < r_{500}$. A larger sample of simulated clusters is needed to determine whether these differences are real.
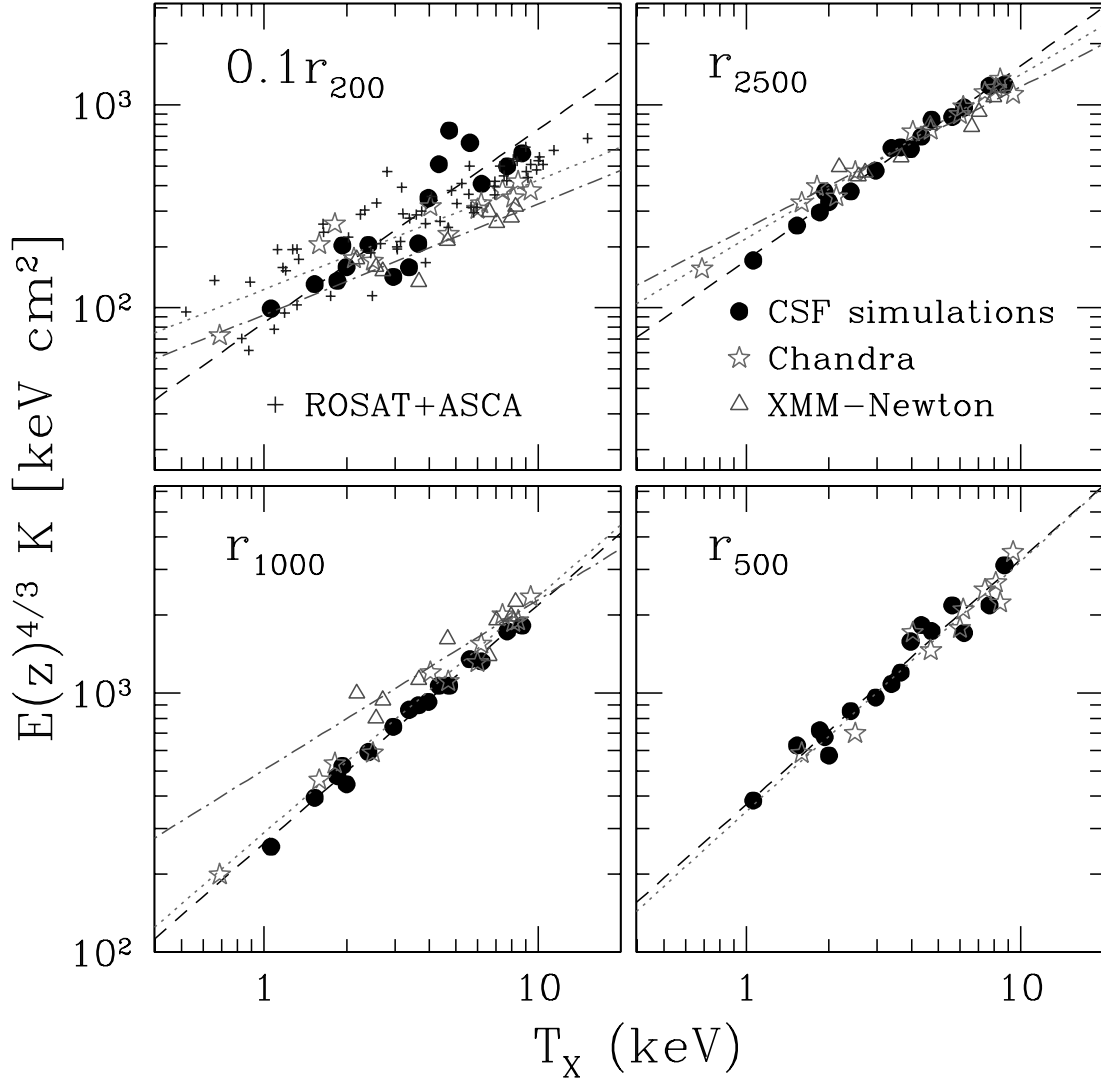
Fig. 4.—Correlation between the entropy $K \equiv k_B T / n_e^{2/3}$ as a function of T_X. The entropy scaling relations are measured at $0.1 r_{200}$, r_{2500}, r_{1000}, and r_{500}. Solid circles indicate the CSF simulations, while stars, triangles, and crosses are *Chandra* (Vikhlinin et al. 2006), *XMM-Newton* (Pratt et al. 2006), and *ROSAT+ASCA* (Ponman et al. 2003) measurements. The dashed, dotted, and dot-dashed lines indicate the best-fit power-law relations to the CSF simulations, *Chandra*, and *XMM-Newton* measurements, respectively. [*See the electronic edition of the Journal for a color version of this figure.*]

It is easier to compare the entropy levels in the simulated and observed clusters via the K-T_X correlation. The results for our CSF runs are $r = 0.1 r_{200}$, r_{2500}, r_{1000}, and r_{500} are shown in Figure 4. Table 3 lists the best-fit parameters of the power approximations, $E(z)^{4/3} K = C (T_X / 5 \text{ keV})^{\alpha}$. As in the case of the K-M relation, the power-law slopes in the CSF runs are slightly shal-

lower than, but consistent with, the self-similar expectation ($\alpha = 1$) at all radii considered. Note also that the K-T_X relations exhibit remarkably tight relations at $r \geq r_{2500}$ for all clusters.

We also show in Figures 3 and 4 the K-M and K-T scalings derived from several sets of X-ray cluster observables. It is most straightforward to compare our simulations with the *Chandra*

TABLE 2
ENTROPY-MASS RELATION

Radius	Quantity	Cooling+SF	Nonradiative	*Chandra*	*XMM-Newton*
$0.1 r_{200}$	$\log C$	2.423 ± 0.030	2.189 ± 0.025	2.391 ± 0.020	2.286 ± 0.033
	α	0.647 ± 0.077	0.774 ± 0.062	0.335 ± 0.046	0.304 ± 0.080
r_{2500}	$\log C$	2.734 ± 0.017	2.516 ± 0.012	2.805 ± 0.011	2.807 ± 0.014
	α	0.593 ± 0.046	0.638 ± 0.031	0.492 ± 0.038	0.407 ± 0.044
r_{1000}	$\log C$	2.890 ± 0.016	2.741 ± 0.017	2.984 ± 0.011	3.094 ± 0.013
	α	0.570 ± 0.043	0.596 ± 0.039	0.569 ± 0.018	0.390 ± 0.046
r_{500}.............................	$\log C$	3.063 ± 0.013	2.936 ± 0.013	3.100 ± 0.013	$\ldots$
	α	0.605 ± 0.036	0.601 ± 0.037	0.598 ± 0.028	$\ldots$

NOTE.—Best-fit parameters for the entropy-mass relation, $E(z)^{2/3} K = C (M_{500} / 2 \times 10^{14} \ h^{-1} \ M_{\odot})^{\alpha}$ at $z = 0$.

TABLE 3
ENTROPY-TEMPERATURE RELATION

Radius	Quantity	Cooling+SF	*Chandra*	*XMM-Newton*
$0.1r_{200}$	$\log C$	2.593 ± 0.042	2.437 ± 0.019	2.320 ± 0.035
	α	0.954 ± 0.077	0.502 ± 0.084	0.506 ± 0.131
r_{2500}	$\log C$	2.905 ± 0.009	2.876 ± 0.013	2.851 ± 0.021
	α	0.958 ± 0.031	0.769 ± 0.054	0.657 ± 0.089
r_{1000}	$\log C$	3.064 ± 0.006	3.067 ± 0.015	3.135 ± 0.026
	α	0.922 ± 0.026	0.887 ± 0.043	0.616 ± 0.106
r_{500}...............	$\log C$	3.232 ± 0.018	3.186 ± 0.018	$\ldots$
	α	0.946 ± 0.060	0.930 ± 0.063	$\ldots$

NOTE.—Best-fit parameters for the entropy-temperature relation $E(z)^{4/3} K = C(T_X/5 \text{ keV})^{\alpha}$ at $z = 0$.

results of Vikhlinin et al. (2006; shown by stars in Figs. 3 and 4), because we explicitly tested their data analysis procedures (Nagai et al. 2007) and because the *Chandra* results for many clusters extend to r_{500}. First, we note the entropy normalizations in the *Chandra* clusters show a good overall agreement with the CSF runs at all radii. The results for nonradiative runs are strongly inconsistent with the data (see also Ponman et al. 2003; Pratt et al. 2006).

At small radii, r_{2500} and $0.1r_{200}$, the observed clusters show significantly shallower slopes than expected in the self-similar model and seen in the simulations. For example, the slope of the K-T relation at $r = 0.1r_{200}$ is $\alpha_{CSF} = 0.95 \pm 0.08$ for the simulated clusters, and $\alpha_{Chandra} = 0.50 \pm 0.08$ for *Chandra* sample. These results are in line with the disagreement between the $K(r)$ profiles of the simulated and observed clusters at small radii, discussed in § 5.1.

The agreement, however, improves quickly as we go to larger radii. At r_{2500}, the slopes of the K-T relation are $\alpha_{CSF} = 0.96 \pm 0.03$ for simulated clusters and $\alpha_{Chandra} = 0.77 \pm 0.05$ for the *Chandra* sample. At larger radii, r_{1000} and r_{500}, the *Chandra*-observed relations are fully consistent with the CSF simulations both in terms of slope and normalization; the slopes are also very close to the self-similar expectations, $\alpha_{K-M} = 2/3$ and $\alpha_{K-T} = 1$. These results confirm the general conclusion of the § 5.1 that although effects of cooling on the entropy normalization are significant within radii as large as r_{500}, the scaling of the thermodynamic properties of the ICM become close to the self-similar expectation outside the inner cluster region.

Also shown in Figures 3 and 4 are the entropy scaling relations derived from two more X-ray data sets, the *XMM-Newton* sample of Pratt et al. (2006; *triangles*) and the *ASCA+ROSAT* sample of Ponman et al. (2003, crosses at $r = 0.1r_{200}$). At small radii, where the X-ray measurements are most straightforward, there is a good agreement between all observed relations. In particular, the *XMM-Newton* and *Chandra* relations for $r = 0.1r_{200}$ and r_{2500} are nearly identical. A small offset of the Ponman et al. (2003) data points can be explained by the slightly different definitions of r_{200} used in these works.[6]

At $r = r_{1000}$, the entropy normalizations for the most massive clusters are in agreement for the *Chandra* and *XMM-Newton* samples but there is some tension in the values of slope. The *XMM-Newton* results indicate nearly the same slopes at $r = r_{1000}$ and smaller radii, all significantly flatter than the self-similar prediction: $\alpha_{K-T} = 0.51 \pm 0.13$, 0.66 ± 0.09, and 0.62 ± 0.11 for $r = 0.1r_{200}$, r_{2500}, and r_{1000}, respectively. The *Chandra* results

clearly indicate a significantly steeper slope at this radius, 0.89 ± 0.04; a steep slope, 0.93 ± 0.06, is also observed at $r = r_{500}$. The statistical significance of the difference between the *Chandra* and *XMM-Newton* slopes is 3.4σ for the K-M and 2.4σ for the K-T relations. The best-fit values of α indicate *qualitatively* different cluster properties. While the *XMM-Newton* results suggest that the departures from self-similar scalings are of the similar amplitude at all radii, the *Chandra* measurements clearly point in the direction that the effect is confined to the very central regions.

A detailed comparison of the *XMM-Newton* and *Chandra* data analyses is beyond the scope of this work. We only point out two effects that may contribute to the difference in the entropy scalings. First, the *Chandra* temperature profiles show a systematic decline at large radii (by a factor of ~ 1.7 at $r = r_{500}$ relative to peak values near $\sim 0.2r_{500}$), the *XMM-Newton* temperature profiles in the Pratt et al. (2006) sample are much flatter. This systematic difference is discussed in Vikhlinin et al. (2005). Second, the gas densities in the *Chandra* analysis were derived using a model that allows for steepening of the $\rho(r)$ profile at large radii. The *XMM-Newton* data were fit with the β-type models that do not allow for such steepening (Pointecouteau et al. 2005). This leads to somewhat different gas density profiles at large radii (see, e.g., Appendix A2 in Vikhlinin et al. 2006).

5.3. *Relations between Total Mass and X-Ray Observables*

We present comparisons of the X-ray observable mass relations of the CSF simulations and *Chandra* X-ray observations of nearby relaxed clusters in Figure 5. Following Kravtsov et al. (2006), we consider three X-ray proxies for the cluster mass: the spectral temperature (T_X), the gas mass (M_g), and the X-ray pressure ($Y_X \equiv T_X M_g$). These X-ray mass proxies are derived from mock *Chandra* images of the simulated clusters and analyzing them using a model and procedure essentially identical to those used in real data analysis. Note that the mean temperatures were estimated from a single temperature to the spectrum integrated in the radial range $[0.15, 1]r_{500}$ (i.e., excluding emission from cluster core).

In the upper panels of Figure 5, we compare the scaling relations of simulated clusters for the true cluster mass, $M_{500}^{\text{true}}(< r_{500}^{\text{true}})$, measured in simulations to the relations from the *Chandra* X-ray cluster observations. We also plot the best-fit M-T_X relation from the *XMM-Newton* measurements (Arnaud et al. 2005) for comparison. Results of power-law fits to these relations for different subsets of the clusters are presented in Table 2 of Kravtsov et al. (2006).[7] The comparisons show that the normalizations of the scaling relations involving true M_{500} for our simulated sample are systematically high by $\approx 10\%$–20% compared to the observed relations. We note that this level of agreement is considerably better than agreement between simulations and data as recently as several years ago (e.g., Pierpaoli et al. 2001).

The remaining bias could arise from the assumption of the hydrostatic equilibrium, which is a key assumption that enables measurements of gravitationally bound mass of clusters from the X-ray and Sunyaev-Zel'dovich (SZ) effect data. To illustrate this, we compare the scaling relations based on the estimated hydrostatic mass [$M_{500}^{\text{HSE}}(< r_{500}^{\text{est}})$] derived from the mock *Chandra* analysis of simulated clusters to the *Chandra* measurements in the lower panels of Figure 5. Note that we account for additional biases in the estimated cluster masses arising from a bias in the estimation of a cluster virial radius by measuring the cluster mass within the r_{500}^{est} estimated from the hydrostatic analysis (see also

---

[6] The quantity r_{200} was defined in Ponman et al. (2003) through the Evrard et al. (1996) scaling with T_X; through the NFW fit to the data at smaller radii in Pratt et al. (2006); and through hydrostatic estimates of r_{500} for the *Chandra* clusters.

[7] Note that M_{500} is in units of $h^{-1} M_{\odot}$ in this work, while it is $M_{\odot}$ in Kravtsov et al. 2006.
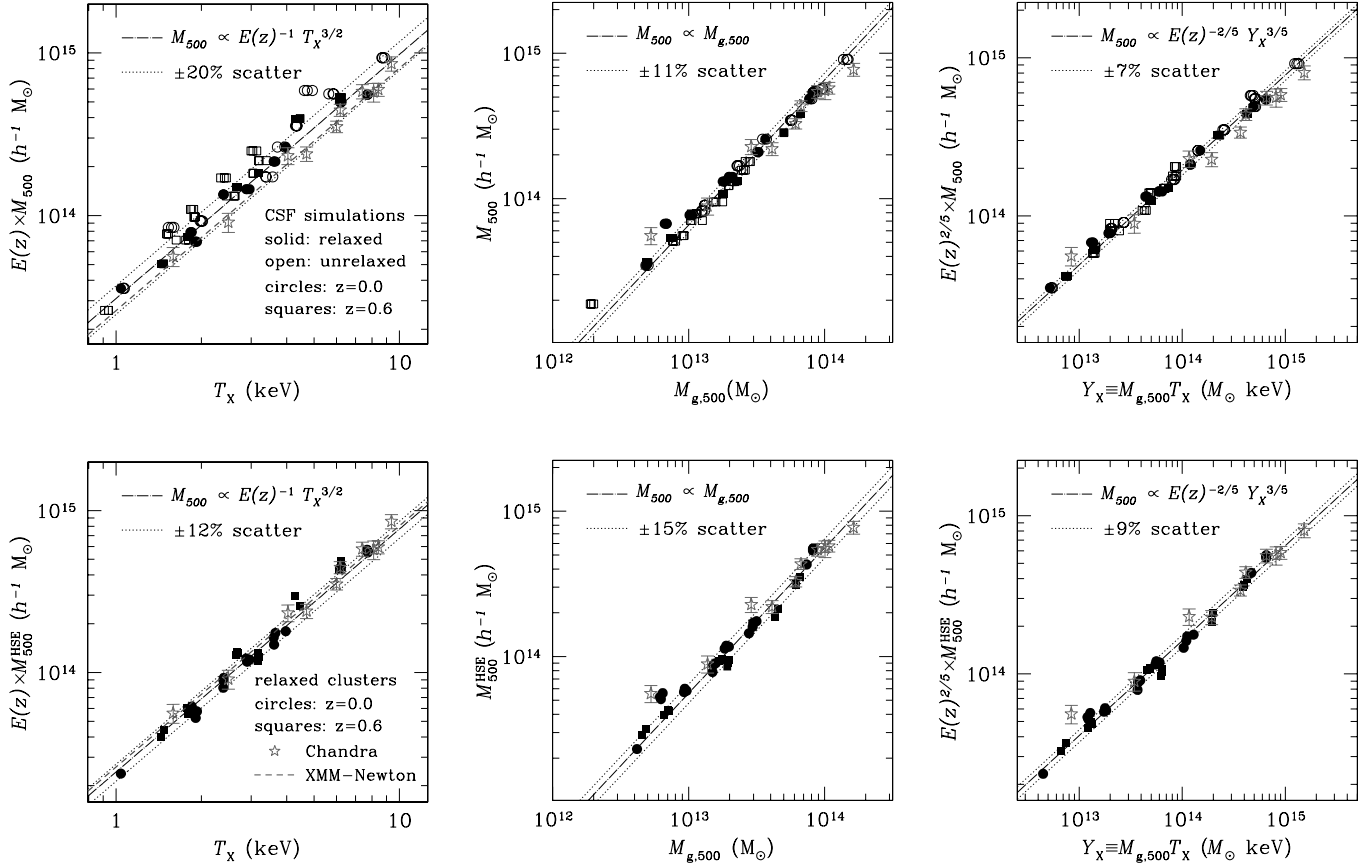
FIG. 5.—Comparisons of the X-ray observable mass relations in simulations and observations. *From left to right*: Correlations between the total mass, M_{500}, and X-ray spectral temperature (T_X), gas mass (M_g), and X-ray pressure ($Y_X \equiv T_X M_g$). Relations are shown for the true 3D cluster mass $M_{500} \equiv M(< r_{500}^{\text{true}})$ as measured in simulations (*top*) and the hydrostatic mass $M_{500}^{\text{HSE}} \equiv M^{\text{HSE}}(< r_{500}^{\text{est}})$ derived from mock *Chandra* analysis (*bottom*). Separate symbols indicate relaxed and unrelaxed simulated clusters, and also $z = 0$ and 0.6 samples. The figures include points corresponding to three projections of each cluster. The dot-dashed lines are the power-law relation with the self-similar slope fit for the sample of relaxed clusters. The dotted lines indicate the rms scatter around the mean relation. The data points with error bars are *Chandra* measurements of nearby relaxed clusters. The dashed line is the best-fit M-T_X relation from the *XMM-Newton* measurements. [*See the electronic edition of the Journal for a color version of this figure.*]

Nagai et al. 2007, for more details and discussions). Similarly, the gas mass ($M_{g,500}$) is also computed at r_{500}^{true} and r_{500}^{est} in the upper and lower panels.[8] In Table 4, we summarize results for the relaxed clusters at $z = 0$, relevant for comparison with observations considered here. These analyses show that the simulation results are in much better agreement with observations when using the hydrostatic mass. The systematic offset in normalizations could thus be due to the bias of total hydrostatic mass estimate due to turbulent motions of the ICM.

In terms of scatter, the M_{500}-T_X relation exhibits the largest scatter of ~20% in M_{500} around the mean relation, most of which is due to unrelaxed clusters. The unrelaxed clusters also have temperatures biased low for a given mass, likely because the mass of the system has already increased but only a fraction of the kinetic energy of merging systems is converted into the thermal energy of gas, due to incomplete relaxation during mergers (Mathiesen & Evrard 2001). Unfortunately, we cannot compare the scatter directly to the *Chandra* results because for real clusters, the scatter is dominated by the measurement uncertainties and the intrinsic scatter (see discussion in Vikhlinin et al. 2006). The slope and redshift evolution of the M_{500}-T_X relations are quite close to the simple self-similar expectation. The M_{500}-M_g relation has a somewhat smaller scatter ($\approx 11\%$) around the best-fit power-law relation than the M_{500}-T_X, but its slope is significantly different from

TABLE 4
MASS VERSUS PROXY RELATIONS

Relation[a]	Quantity[b]	M_{500}^{SIM} (True)	M_{500}^{SIM} (HSE)	M_{500} (*Chandra*)
M_{500}-T_X	$\log C$	14.21 ± 0.010	14.10 ± 0.008	14.11 ± 0.035
	α	1.515 ± 0.052	1.623 ± 0.027	1.489 ± 0.093
	Scatter	0.136	0.117	...
	$\log C_{ss}$	14.21 ± 0.009	14.10 ± 0.009	14.10 ± 0.014
M_{500}-M_g	$\log C$	14.12 ± 0.008	14.05 ± 0.011	14.14 ± 0.044
	α	0.894 ± 0.023	0.932 ± 0.033	0.811 ± 0.067
	Scatter	0.114	0.153	...
	$\log C_{ss}$	14.12 ± 0.010	14.05 ± 0.011	14.07 ± 0.022
M_{500}-Y_X	$\log C$	14.06 ± 0.004	13.97 ± 0.007	14.04 ± 0.047
	α	0.568 ± 0.006	0.596 ± 0.010	0.526 ± 0.038
	Scatter	0.053	0.087	...
	$\log C_{ss}$	14.05 ± 0.005	13.97 ± 0.006	13.98 ± 0.017

NOTE.—Best-fit parameters and scatter in the mass vs. proxy relations, $M_{500} = CX^\alpha$, for relaxed clusters at $z = 0$ and 0.6.

[a] Power-law fits were performed for relaxed clusters of our cluster sample at $z = 0$ and 0.6. In addition to the fits in which both the normalization and the slope of the power-law relations were fit simultaneously, we provide the best-fit normalizations, C_{ss}, for each relation when fit with the slopes fixed to their self-similar values: 1.5, 1.0, and 0.6 for the M_{500}-T_X, M_{500}-M_g, and M_{500}-Y_X relations, respectively.

[b] For each observable $X (= T_X, M_g, Y_X)$, we fit power-law relation of the form $M_{500} = C(X/X_0)^\alpha$ with $X_0 = 3.0$ keV, $2 \times 10^{13} M_\odot$, and 4×10^{13} keV $M_\odot$, for T_X, M_g, Y_X, respectively. Note that M_{500} is in units of $h^{-1} M_\odot$.

---

[8] Note that T_X is computed within r_{500}^{true} in both panels; however, correcting for the bias in r_{500} has a negligible ($\lesssim 1\%$) effect on the T_X estimate.

the self-similar prediction for the M_{500}-M_g relation due to the trend of gas fraction with cluster mass present for both the simulated clusters in our sample (see Kravtsov et al. 2005) and for the observed clusters (Vikhlinin et al. 2006). In all of the scaling relations considered here, the use of $M_{500}^{\rm HSE}$, instead of $M_{500}^{\rm true}$, modifies the scatter by a few percent for the relaxed clusters.

The M_{500}-$Y_{\rm X}$ relation shows the scatter of only $\approx 7\%$, making it by far the tightest of all the scaling relations. Note that this value of scatter includes clusters at both low and high redshifts and both relaxed and unrelaxed systems. The tightness of the M_{500}-$Y_{\rm X}$ relation and simple evolution are due to a fortunate cancellation of opposite trends in gas mass and temperature (see Kravtsov et al. 2006). The slope and redshift evolution of normalization for the M_{500}-$Y_{\rm X}$ relations are well described by the simple self-similar model.

6. DISCUSSION AND CONCLUSIONS

We presented analyses of the simulated cluster sample of 16 clusters spanning a representative mass range (5×10^{13}–$2 \times 10^{15}~h^{-1}~M_\odot$) and modeled using the shock-capturing Eulerian adaptive mesh refinement N-body+gas dynamics ART code in the ΛCDM cosmology. These simulations achieve high spatial resolution and include various physical processes of galaxy formation, including radiative cooling, star formation, and other processes accompanying galaxy formation. We study the effects of gas cooling and star formation on the ICM properties by comparing two sets of simulations performed with and without these processes included. The results of simulations with dissipation are compared to recent *Chandra* X-ray observations of nearby, relaxed clusters (Vikhlinin et al. 2005, 2006).

We show that gas cooling and star formation modify both the normalization and the shape of the gas density, temperature, entropy, and pressure profiles. As the lowest entropy gas cools and condenses out of the hot phase in the cluster progenitors, the gas density in their inner regions is lowered and entropy is increased (Bryan 2000; Voit & Bryan 2001). The effects have strong radial dependence and are the strongest in the inner regions $r \lesssim 0.1 r_{500}$. At these inner radii simulation profiles do not match the observations. On the other hand, at $r \gtrsim 0.1 r_{500}$ the profiles in the CSF simulations and observations agree quite well, while profiles in the nonradiative runs disagree with observations at all radii within r_{500}.

In particular, the simulations with cooling can explain the observed high levels of entropy in observed clusters compared to the nonradiative expectation pointed out previously (Ponman et al. 2003; Pratt et al. 2006). At $r \gtrsim r_{2500}$, the cluster profiles are approximately self-similar within current statistical error bars, while there is an indication that their best-fit slopes are slightly shallower than the self-similar value. Moreover, the slope and normalization of the entropy scaling relations in the simulated clusters are in good agreement with *Chandra* observations at r_{1000} and r_{500}, while the observed relations exhibits deviations from the self-similarity at $r \lesssim r_{2500}$. Note also that the results of *Chandra* and *XMM-Newton* measurements agree quite well within $r \lesssim r_{2500}$, but the significant disagreement is seen at r_{1000}. The statistical significance of the difference between the *Chandra* and *XMM-Newton* slopes is $3.4\,\sigma$ for the K-M and $2.4\,\sigma$ for the K-T relations. The difference is critical for theoretical interpretation and implications, as the *XMM-Newton* scaling was billed as a major evidence for deviations from self-similar scalings at large radii (indeed at r_{1000}, where *XMM-Newton* measurements is several sigma away from the slope of 1.0). *Chandra* results show that deviations at larger radii, if they exist, are much smaller. Despite the deviations from self-similarity in the ICM entropies, we show that pressure profiles, in particular, show a remarkable degree of self-similarity and exhibit very small scatter.

We also present comparisons of scaling relations of cluster X-ray observables with total cluster mass in the simulations with cooling and recent deep *Chandra* observations. Specifically, we compare correlation of the spectral X-ray temperature, ICM gas mass (M_g), and the X-ray equivalent of integrated pressure ($Y_{\rm X} \equiv M_g T_{\rm X}$). In these comparisons X-ray observables for the simulated clusters are derived from mock *Chandra* analysis using procedure essentially identical to those used in real data analysis.

The slope and normalization of the M-$T_{\rm X}$ and M-$Y_{\rm X}$ relations in simulations and *Chandra* observations are in good agreement, and they are consistent with the simple self-similar expectation. In terms of scatter, the M_{500}-$Y_{\rm X}$ relation shows scatter of only $\approx 7\%$, making it by far the tightest of all the scaling relations. Note that this value of scatter includes clusters at both low and high redshifts and both relaxed and unrelaxed systems. The M_{500}-$T_{\rm X}$ relation, on the other hand, exhibits the largest scatter of $\sim 20\%$ scatter in M_{500} around the mean relation, most of which is due to unrelaxed clusters. The unrelaxed clusters also have temperatures biased low for a given mass, likely because the mass of the system has already increased but only a fraction of the kinetic energy of merging systems is converted into the thermal energy of gas, due to incomplete relaxation (Mathiesen & Evrard 2001) during mergers.

Moreover, these comparisons show that the normalizations of the scaling relations of relaxed clusters in simulations and observations agree at a level of about $\approx 10\%$–20%. This is a considerable improvement, given that significant disagreement existed just several years ago (see Finoguenov et al. 2001; Seljak 2002; Pierpaoli et al. 2003). The residual systematic offset in the normalization is likely caused by nonthermal pressure support from subsonic turbulent gas motions (Evrard et al. 1996; Rasia et al. 2004, 2006; Faltenbacher et al. 2005; Dolag et al. 2005; E. Lau et al. 2007, in preparation). This contribution is approximately independent of cluster mass (Vazza et al. 2006; E. Lau et al. 2007, in preparation) and is not accounted for in X-ray hydrostatic mass estimates. For example, when we repeat the comparison of scaling relations using hydrostatic mass estimates for the observed clusters, we find excellent agreement in normalizations, demonstrating explicitly that there is a systematic $\approx 10\%$–20% offset between hydrostatic mass estimate and the true mass in simulated clusters.

Part of the nonthermal pressure support may also be contributed by cosmic rays and magnetic fields. In practice, it may be difficult to distinguish between different sources of nonthermal pressure. A possible test is their radial dependence. Turbulent motions, for example, are in general smaller at smaller radii and the turbulent pressure gradient is correspondingly smaller. In the case of turbulent motions, we can therefore expect that the bias in the total mass estimate should decrease at smaller radii. This may not be the case for some other sources of nonthermal pressure, although recent models of cosmic rays contribution to the total pressure show a qualitatively similar radial dependence as the turbulent pressure (Pfrommer et al. 2007)

The much improved agreement of the scaling relations and especially normalization and shape of the gas profiles between simulations with cooling and star formation and observations show that inclusion of galaxy formation in cluster simulations results in more realistic modeling of the hot ICM. This may indicate that gravitational dynamics and the basic cooling of the hot gas accompanying galaxy formation are the dominant processes determining thermodynamics of the ICM outside the cluster cores, while other processes, such as feedback, thermal conduction, viscosity, and cosmic rays, are playing only a minor role for a large fraction of the ICM mass.

Note, however, that the agreement between our simulations and observations is achieved by condensation of a significant fraction of hot gas into cold dense phase, which is subsequently converted into stars. Thus, simulated clusters have $\approx 40\%$ of their baryons within r_{500} in stellar form at $z = 0$, while the rest of the baryons are in the hot phase. Although the low hot gas mass fractions ($\approx 60\%-70\%$ of the universal value) are consistent with observations (Vikhlinin et al. 2006; McCarthy et al. 2007), the high stellar fractions are not. Note, however, that the reduced stellar fraction with more efficient stellar or AGN energy feedback generally results in the profiles that are in between those of the CSF and nonradiative runs and disrupts the good agreement between models and data.

Observational estimates of the stellar mass fractions in groups and clusters range from $\approx 5\%-10\%$ (Eke et al. 2005) to $\approx 15\%-20\%$ (Lin et al. 2003; Gonzalez et al. 2007) of the universal baryon fraction or at least a factor of 2–3 lower than the fractions found in our simulations. This is a well-known discrepancy often referred to as the "overcooling problem." Our results show that the X-ray and optical observations appear to give seemingly contradicting constraints. The low observed stellar fractions imply existence of an efficient mechanism suppressing star formation in real clusters, while observed properties of hot ICM are not consistent with small amounts of cooling (i.e., predictions close to the nonradiative limit). At present it is not clear how these two observational constraints can be reconciled.

Our tests indicate that profiles and average quantities (i.e., gas fractions) derived from analyses of modern X-ray data are robust and do not suffer any obvious biases (Nagai et al. 2007). On the other hand, there are certain systematic uncertainties in estimates of stellar mass from optical observations related both to possible low surface stellar component missed in shallow observations (e.g., Gonzalez et al. 2005, 2007; Lauer et al. 2007; Seigar et al.

2007) and to the uncertainties in the stellar population modeling of the observed photometry. It is unlikely, however, that any single uncertainty is large enough to account for the entire factor of 2–3 discrepancy between stellar fractions in simulations and observations. We note also that stellar fraction predicted by simulations depends on the implementation of the feedback processes in simulations (e.g., Borgani et al. 2006). However, the current implementations of the feedback processes efficient in significantly suppressing stellar fraction are essentially ad hoc, and it is uncertain whether the feedback is actually as efficient in practice.

The progress in our understanding of these issues should come from detailed convergence studies and comparisons of simulation results done using different numerical codes, further comparisons of simulations with deep X-ray observations, deeper observations, and thorough analysis of uncertainties in the optical estimates of cluster stellar masses.

APPENDIX

ANALYTIC PRESSURE MODEL

The Sunyaev-Zel'dovich (SZ) effect is a direct probe of thermal energy content of the universe and provides a unique and powerful probe of the structure formation and cosmology in the near future. The SZ observations are probing the integrated pressure of the ICM.
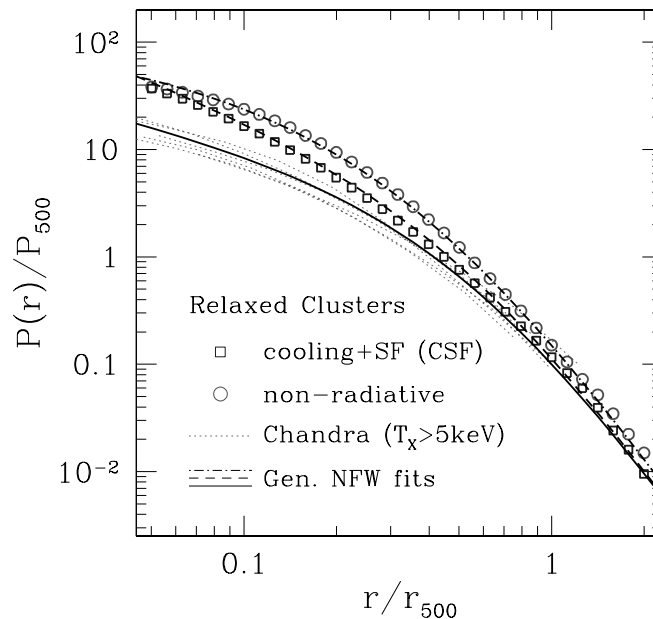

FIG. 6.—Generalized NFW fits to the pressure profiles of relaxed clusters in simulations and *Chandra* X-ray observations. Open circles and squares show the mean profiles in the CSF and nonradiative simulations, respectively. Thin dotted shows *Chandra* X-ray clusters with $T_X > 5$ keV. Thick lines show the best-fit generalized NFW model to simulation and observed profiles (see Table 5 for the best-fit parameters). [*See the electronic edition of the Journal for a color version of this figure.*]

TABLE 5
Best-Fit Parameters of the Pressure Profile

Runs	Sample	P_0	c_{500}	(α, β, γ)
Chandra observations..................	Relaxed	3.3	1.8	(1.3,4.3,0.7)
Cooling+SF................................	Relaxed	3.3	1.8	(1.3,4.3,1.1)
	Unrelaxed	2.0	1.5	(1.4,4.3,1.0)
Nonradiative................................	Relaxed	38.0	3.0	(1.1,4.3,0.3)
	Unrelaxed	3.0	1.5	(1.4,4.3,0.9)

Accurate analytic parameterizations of the ICM pressure profiles can therefore be useful for developing efficient cluster detection algorithm for upcoming SZ cluster surveys, analysis, and interpretation of SZ effect observations, as well as theoretical modeling of cluster ICM. The fact that the self-similarity is best preserved for the pressure profiles and their low cluster-to-cluster scatter (see § 4) provides further motivation for the use of accurate pressure profile parameterizations.

Here we present a simple analytic model of the pressure profile that closely matches the observed profiles of the *Chandra* X-ray clusters and results of numerical simulations in their outskirts. Since the gas pressure distribution is primarily determined by the gravitationally dominant dark matter component, we parameterize the pressure profile using the generalized NFW model,

$$\frac{P(r)}{P_{500}} = \frac{P_0}{x^\gamma (1+x^\alpha)^{(\beta-\gamma)/\alpha}}, \tag{A1}$$

where $x \equiv r/r_s$, $r_s = r_{500}/c_{500}$, P_{500} is given by equation (3), and (α, β, γ) are the slopes at $r \sim r_s$, $r \gg r_s$, and $r \ll r_s$, respectively. We find that a model with $P_0 = 3.3$, $c_{500} \equiv r_{500}/r_s = 1.8$, and $(\alpha, \beta, \gamma) = (1.3, 4.3, 0.7)$ provides a good description of the pressure profiles of the high-T_X *Chandra* clusters within the observed range ($r \lesssim r_{500}$), as well as the profiles of simulated clusters in $0.5 < r/r_{500} < 2.0$. Figure 6 shows generalized NFW fits to the pressure profiles of relaxed clusters in simulations and *Chandra* observations. In the outskirts, we set the slope to be $\gamma = 4.3$, which is the average best-fit values for both nonradiative and CSF simulations. For the *Chandra* clusters with $T_X > 5$ keV, the inner slopes of the pressure profile are ≈ 0.7. The inner slopes appear to be shallower for the lower T_X systems, but they also show much larger cluster-to-cluster variation. Table 5 summarizes the best-fit model parameters for observed and simulated clusters. For the relaxed systems, the same set of parameters with a different inner slope $\gamma = 1.1$ produces the pressure profile of the CSF run, while that of the nonradiative run requires a very different set of parameters. The pressure profiles of the unrelaxed systems are generally less concentrated (smaller value of c_{500}) with slightly different inner and outer slopes.

REFERENCES

Albrecht, A., et al. 2006, preprint (astro-ph/0609591)
Allen, S. W., & Fabian, A. C. 1998, MNRAS, 297, L57
Allen, S. W., Schmidt, R. W., Ebeling, H., Fabian, A. C., & van Speybroeck, L. 2004, MNRAS, 353, 457
Arnaud, M., & Evrard, A. E. 1999, MNRAS, 305, 631
Arnaud, M., Pointecouteau, E., & Pratt, G. W. 2005, A&A, 441, 893
Ascasibar, Y., Yepes, G., Müller, V., & Gottlöber, S. 2003, MNRAS, 346, 731
Bialek, J. J., Evrard, A. E., & Mohr, J. J. 2001, ApJ, 555, 597
Borgani, S. 2006, in Lectures for 2005 Guillermo Haro Summer School on Clusters (Berlin: Springer), preprint (astro-ph/0605575)
Borgani, S., Governato, F., Wadsley, J., Menci, N., Tozzi, P., Lake, G., Quinn, T., & Stadel, J. 2001, ApJ, 559, L71
Borgani, S., Governato, F., Wadsley, J., Menci, N., Tozzi, P., Quinn, T., Stadel, J., & Lake, G. 2002, MNRAS, 336, 409
Borgani, S., et al. 2006, MNRAS, 367, 1641
Brüggen, M., Ruszkowski, M., & Hallman, E. 2005, ApJ, 630, 740
Bryan, G. L. 2000, ApJ, 544, L1
Cattaneo, A., & Teyssier, R. 2007, MNRAS, 376, 1547
Clowe, D., Bradač, M., Gonzalez, A. H., Markevitch, M., Randall, S. W., Jones, C., & Zaritsky, D. 2006, ApJ, 648, L109
Davé, R., Katz, N., & Weinberg, D. H. 2002, ApJ, 579, 23
David, L. P., Forman, W., & Jones, C. 1991, ApJ, 380, 39
De Grandi, S., & Molendi, S. 2002, ApJ, 567, 163
Dolag, K., Vazza, F., Brunetti, G., & Tormen, G. 2005, MNRAS, 364, 753
Edge, A. C., & Stewart, G. C. 1991, MNRAS, 252, 414
Eke, V. R., Baugh, C. M., Cole, S., Frenk, C. S., King, H. M., & Peacock, J. A. 2005, MNRAS, 362, 1233
Ettori, S., et al. 2004, MNRAS, 354, 111
Evrard, A. E. 1990, ApJ, 363, 349
Evrard, A. E., & Henry, J. P. 1991, ApJ, 383, 95
Evrard, A. E., Metzler, C. A., & Navarro, J. F. 1996, ApJ, 469, 494
Faltenbacher, A., Kravtsov, A. V., Nagai, D., & Gottlöber, S. 2005, MNRAS, 358, 139
Ferland, G. J., Korista, K. T., Verner, D. A., Ferguson, J. W., Kingdon, J. B., & Verner, E. M. 1998, PASP, 110, 761
Finoguenov, A., Jones, C., Böhringer, H., & Ponman, T. J. 2002, ApJ, 578, 74

Finoguenov, A., Ponman, T. J., Osmond, J. P. F., & Zimer, M. 2007, MNRAS, 374, 737
Finoguenov, A., Reiprich, T. H., & Böhringer, H. 2001, A&A, 368, 749
Frenk, C. S., et al. 1999, ApJ, 525, 554
Gonzalez, A. H., Zabludoff, A. I., & Zaritsky, D. 2005, ApJ, 618, 195
Gonzalez, A. H., Zaritsky, D., & Zabludoff, A. I. 2007, ApJ, in press (arXiv: 0705.1726)
Haardt, F., & Madau, P. 1996, ApJ, 461, 20
Helsdon, S. F., & Ponman, T. J. 2000, MNRAS, 319, 933
Henry, J. P., & Arnaud, K. A. 1991, ApJ, 372, 410
Ikebe, Y., Reiprich, T. H., Böhringer, H., Tanaka, Y., & Kitayama, T. 2002, A&A, 383, 773
Kaiser, N. 1986, MNRAS, 222, 323
———. 1991, ApJ, 383, 104
Kay, S. T., da Silva, A. C., Aghanim, N., Blanchard, A., Liddle, A. R., Puget, J.-L., Sadat, R., & Thomas, P. A. 2007, MNRAS, 377, 317
Kay, S. T., Thomas, P. A., Jenkins, A., & Pearce, F. R. 2004, MNRAS, 355, 1091
Kennicutt, R. C. 1998, ApJ, 498, 541
Klypin, A., Kravtsov, A. V., Bullock, J. S., & Primack, J. R. 2001, ApJ, 554, 903
Kravtsov, A. V. 1999, Ph.D. thesis, New Mexico State Univ.
Kravtsov, A. V., Klypin, A., & Hoffman, Y. 2002, ApJ, 571, 563
Kravtsov, A. V., Nagai, D., & Vikhlinin, A. A. 2005, ApJ, 625, 588
Kravtsov, A. V., Vikhlinin, A., & Nagai, D. 2006, ApJ, 650, 128
LaRoque, S. J., Bonamente, M., Carlstrom, J. E., Joy, M. K., Nagai, D., Reese, E. D., & Dawson, K. S. 2006, ApJ, 652, 917
Lauer, T. R., et al. 2007, ApJ, 662, 808
Lewis, G. F., Babul, A., Katz, N., Quinn, T., Hernquist, L., & Weinberg, D. H. 2000, ApJ, 536, 623
Lin, Y.-T., Mohr, J. J., & Stanford, S. A. 2003, ApJ, 591, 749
Markevitch, M. 1998, ApJ, 504, 27
Markevitch, M., Gonzalez, A. H., Clowe, D., Vikhlinin, A., Forman, W., Jones, C., Murray, S., & Tucker, W. 2004, ApJ, 606, 819
Markevitch, M., et al. 2003, ApJ, 586, L19
Mathiesen, B. F., & Evrard, A. E. 2001, ApJ, 546, 100

McCarthy, I. G., Bower, R. G., & Balogh, M. L. 2007, MNRAS, 377, 1457
Metzler, C. A., & Evrard, A. E. 1994, ApJ, 437, 564
Miller, C. J., Nichol, R. C., & Chen, X. 2002, ApJ, 579, 483
Muanwong, O., Thomas, P. A., Kay, S. T., Pearce, F. R., & Couchman, H. M. P. 2001, ApJ, 552, L27
Nagai, D. 2006, ApJ, 650, 538
Nagai, D., Kravtsov, A. V., & Kosowsky, A. 2003, ApJ, 587, 524
Nagai, D., Vikhlinin, A. A., & Kravtsov, A. V. 2007, ApJ, 655, 98
Nath, B. B., & Roychowdhury, S. 2002, MNRAS, 333, 145
Norman, M. L., & Bryan, G. L. 1999, in The Radio Galaxy Messier 87, ed. H.-J. Röser & K. Meisenheimer (New York: Springer), 106
Pearce, F. R., Thomas, P. A., Couchman, H. M. P., & Edge, A. C. 2000, MNRAS, 317, 1029
Pfrommer, C., Ensslin, T. A., Springel, V., Jubelgas, M., & Dolag, K. 2007, MNRAS, 378, 385
Pierpaoli, E., Borgani, S., Scott, D., & White, M. 2003, MNRAS, 342, 163
Pierpaoli, E., Scott, D., & White, M. 2001, MNRAS, 325, 77
Pointecouteau, E., Arnaud, M., & Pratt, G. W. 2005, A&A, 435, 1
Ponman, T. J., Cannon, D. B., & Navarro, J. F. 1999, Nature, 397, 135
Ponman, T. J., Sanderson, A. J. R., & Finoguenov, A. 2003, MNRAS, 343, 331
Pratt, G. W., Arnaud, M., & Pointecouteau, E. 2006, A&A, 446, 429
Rasia, E., Tormen, G., & Moscardini, L. 2004, MNRAS, 351, 237
Rasia, E., et al. 2006, MNRAS, 369, 2013
Seigar, M. S., Graham, A. W., & Jerjen, H. 2007, MNRAS, 378, 1575
Seljak, U. 2002, MNRAS, 337, 769
Sijacki, D., & Springel, V. 2006, MNRAS, 366, 397
Suginohara, T., & Ostriker, J. P. 1998, ApJ, 507, 16
Tozzi, P. 2006, in Lectures in the 3rd Aegean Summer School, preprint (astro-ph/0602072)
Valdarnini, R. 2002, ApJ, 567, 741
———. 2003, MNRAS, 339, 1117
Vazza, F., Tormen, G., Cassano, R., Brunetti, G., & Dolag, K. 2006, MNRAS, 369, L14
Vikhlinin, A. 2006, ApJ, 640, 710
Vikhlinin, A., Kravtsov, A., Forman, W., Jones, C., Markevitch, M., Murray, S. S., & Van Speybroeck, L. 2006, ApJ, 640, 691
Vikhlinin, A., Markevitch, M., & Murray, S. S. 2001a, ApJ, 551, 160
———. 2001b, ApJ, 549, L47
Vikhlinin, A., Markevitch, M., Murray, S. S., Jones, C., Forman, W., & Van Speybroeck, L. 2005, ApJ, 628, 655
Vikhlinin, A., et al. 2003, ApJ, 590, 15
Voit, G. M. 2005, Rev. Mod. Phys., 77, 207
Voit, G. M., & Bryan, G. L. 2001, Nature, 414, 425
Voit, G. M., Bryan, G. L., Balogh, M. L., & Bower, R. G. 2002, ApJ, 576, 601
Voit, G. M., Kay, S. T., & Bryan, G. L. 2005, MNRAS, 364, 909
White, D. A., Jones, C., & Forman, W. 1997, MNRAS, 292, 419
White, R. E., III 1991, ApJ, 367, 69
Wu, K. K. S., Fabian, A. C., & Nulsen, P. E. J. 2000, MNRAS, 318, 889